Synthesis of MnM-NC (M=Ga, In, Sn) Dual-single-atom Catalysts for Efficient Electrocatalytic Oxygen Reduction†

Yujie Cui, [‡a] Yihong Liu, [‡a] Jiayi Li, [a] Haibin Ma, [a] Tingting Pan, [a] Hainan Wei, [a] Xinyue Shi, [a] Xiaoyan Zhou, [a] Ping Zhang, [a] Weixing Niu, [a] Shengnan Sun, [b] Menghao Yang, [a] Wei-Hsiang Huang, [*cd] Jiwei Ma [a] and Hongfei Cheng [*a]

a. Shanghai Key Laboratory for R&D and Application of Metallic Functional Materials, Institute of New Energy for Vehicles, School of Materials Science and Engineering, Tongji University, Shanghai 201804, China. E-mail: cheng_hongfei@tongji.edu.cn

b. Institute of Materials Research and Engineering (IMRE), Agency for Science, Technology and Research (A*STAR), 2 Fusionopolis Way, Innovis #08-03, Singapore 138634, Republic of Singapore.

c. National Synchrotron Radiation Research Center (NSRRC), Hsinchu, 300092, Taiwan.

d. Sustainable Electrochemical Energy Development (SEED) Center, National Taiwan University of Science and Technology, Taipei 106, Taiwan. E-mail: huang.sean@nsrrc.org.tw

*. Corresponding authors

† Supplementary Information available. See DOI: 10.1039/x0xx00000x

‡ These authors contributed equally to this work.

Oxygen reduction reaction (ORR) is an important reaction in the field of energy conversion and storage. Manganese-based catalysts are expected to be alternative candidates to iron-based or platinum-group catalysts by virtue of their low cost, good stability and resistance to Fenton reaction. The easily tunable localized p-orbitals of p-block metals and the d-orbitals of manganese can hybridize, which facilitates the oxygen reduction process. Here, we have designed and synthesized a series of dual-single-atom catalysts that consist of Mn and p-block metal single atoms dispersed on N-doped carbon, denoted as MnM-NC (M=Ga/In/Sn). After introducing p-block metal single atoms, the half-wave potential of the catalysts increases to 0.85 V (vs. RHE), and the stability is also improved and even better than that of commercial Pt/C. Theoretical calculations show that the dual-single-atom sites could adjust the d-band center of the Mn site, weakening the adsorption strength of the intermediate *OH, thus improving the ORR catalytic activity. This work provides insights into the coupling of Mn-NC species materials with p-block metals to improve ORR performance, as well as inspires more structural and application innovations of p-block metals in the ORR research field.

1. Introduction

Electrocatalytic oxygen reduction reaction (ORR) is a key to the overall efficiency of the emerging energy storage and conversion devices, such as fuel cells[1-3], and metal-air batteries[4]. Platinum group catalysts are still the best choice for ORR[5-7], but their high cost and low reserves hinder the wide application. Thereby single-atom catalysts (SACs) especially carbon nanomaterials doped with nitrogen and transition metal single atoms, have gained notable attention for ORR[8, 9], among which Fe-N-C nanomaterials show good performance comparable to Pt/C in alkaline conditions. However, Fe-N-C nanomaterials suffer from poor stability due to the inevitable Fenton reaction[10]. Alternatively, Mn-based materials, where the Mn is also an abundant and inexpensive metal, have been demonstrated to be promising ORR catalyst candidates[11-15]. Mn-N-C materials have been proved by theoretical

calculations to have comparable performance to that of Fe-N-C[16], with the absence of the Fenton reaction and better durability[17, 18]. To improve the performance of Mn-N-C materials for commercial applications, introducing non-metallic atoms such as B[19], P[20], S[21, 22], and O[23-25] and a second transition metal, such as Fe[26-29], Co[30], are two common strategies, which can break local structural symmetry and induce charge redistribution, thus optimizing the adsorption energy of oxygen intermediates.

In addition to the commonly studied *d*-block metals, recent studies have demonstrated the electrocatalytic feasibility of main-group elements for ORR, such as *p*-block metal single atom sites[31-37]. The *p*-*d* orbital hybridization arising from *p*-metal and *d*-metal helps to adjust the adsorption strength of electrocatalytic intermediates[38, 39], based on which *d*-*p* dual-single-atom pairs such as Fe-Sn[40, 41], Fe-Sb[42] and Fe-Al[43] have been developed. However, the coupling of *p*-block metals with Mn single atoms has not been reported.
Inspired by the above works, we develop Mn-N-C SACs doped with atomically dispersed *p*-block metals, including Ga, In and Sn, and demonstrate that all of these *p*-block metals can improve the ORR activity. Theoretical calculations show that *p*-block metal single-atom sites can adjust the *d*-band center of the Mn single-atom site through *p*-*d* orbital hybridization, thus attenuating the over-adsorption of *OH.

2. Results and discussion

2.1 Morphology and structure characterization

The catalysts with dual-single-atom structure were obtained by a two-step pyrolysis method[44], which is shown in **Fig. 1a**. Firstly, ZIF-8 precursor with good crystallinity was synthesized (**Fig. S1**), and underwent pyrolysis to obtain the nitrogen-doped carbon (NC). Two very broad XRD peaks centered at ~25°and ~43°can be attributed to the (002) and (101) crystal planes of carbon[45] (**Fig. 1b**), indicating that the obtained NC has ordered graphitic structure in short range but disordered in long range . Subsequently, Mn ions and *p*-block metal ions were adsorbed onto NC, and then secondary pyrolysis was performed to obtain dual-single-atom catalysts, denoted as MnM-NC (M=Ga/In/Sn). The Mn-N-C was also prepared by following the same procedures without adding *p*-block metal precursors. The XRD patterns of the catalysts only show the characteristic peaks of carbon when the *p*-block metal content is lower than the Mn (**Fig. 1b, S2-4**), therefore it is speculated that all the metal sites in these catalysts are atomically dispersed. By tuning the content of the *p*-block metal precursors, it was found that when the *p*-block metal accounted for 15 wt%, the ORR activity reached the optimal (**Fig. S5-8**). Hence, in the following discussions, the *p*-block metal is 15 wt% for all the MnM-NC catalysts unless otherwise specified.

The SEM images show that the ZIF-8 has a typical rhombic dodecahedron shape with good uniformity and NC showed a similar morphology (**Fig. S9**). The pore structure on the NC surface could be observed. After introducing the metal precursors and secondary pyrolysis, the morphology of the products was still well preserved (**Fig. 1c**). Transmission electron microscopy (TEM) images of the MnGa-NC show a morphology similar to the ZIF-8 (**Fig. S10**), and no Mn or Ga agglomerates were observed (**Fig. 2a, S11**). The high-resolution TEM image of MnGa-NC (**Fig. S12**) shows a worm-like characteristic of amorphous carbon. TEM-energy dispersive X-ray spectroscopy (EDS) mappings (**Fig. 2b**, **S13**) show a uniform distribution of the elements Mn, Ga and N.

A more in-depth fine characterization was carried out in order to visualize the presence of single atoms as well as the potential dual-single-atom structure. For this purpose, aberration-corrected high-angle annular dark-field scanning TEM (AC-HAADF-STEM) images were collected. Mn-NC and MnGa-NC were selected as representative samples for comparison. Due to the higher atomic number of Mn and Ga compared to carbon and nitrogen, they appear as bright spots on the images. **Fig. 2c-d** show the AC-HAADF-STEM images of the Mn-NC sample, where the monatomic Mn sites are indicated by red dashed circles. **Fig. 2e-f** show the AC-HAADF-STEM images of the MnGa-NC sample, where the potential dual-single-atom sites are marked by orange rectangular dashed boxes. Comparisons of more regions are provided in **Fig. S14-24** to illustrate the atomic dispersion of metal elements. Comparing the AC-HAADF-STEM images of Mn-NC and MnGa-NC, it can be visually observed that the MnGa-NC has a higher density of atomic metal sites. This may be due to the interaction between Mn and Ga, which would facilitate their anchoring on the substrate. The typical regions **#1** and **#2** from Mn-NC and MnGa-NC were subsequently selected to be enlarged and more intuitively illustrated in 2D and 3D forms (**Fig. S25**). The bright spots in **#1** are more widely spaced and are considered to be isolated monatomic sites. The bright spots in **#2** are more compact and can be empirically considered as potential dual-single-atom sites, which may exist in the form of Mn-Ga, Ga-Ga or Mn-Mn based on the metal precursor casting. More brightness line profile analysis was performed to demonstrate the dual-single atom sites (**Fig. S26**). The metal loading in each single-atom sample was also measured by inductively coupled plasma emission spectroscopy (ICP-OES), as summarized in **Table S1**. the Mn and Ga contents in MnGa-NC were 2.41 wt% and 0.42 wt%, which is consistent with the Ga cast of 15 wt%. The Mn and In contents in MnIn-NC were 2.16 wt% and 0.37 wt%, and the contents of Mn and Sn in MnSn-NC are 2.33 wt% and 0.35 wt%, respectively. The loadings are similar and all of them are in accordance with the cast. The Mn content in Mn-NC is 1.80% and the metal loading is less than that of samples doped with *p*-block metals, which is also consistent with the AC-HAADF-STEM image comparison. In conclusion, monoatomic Mn and dual-single-atom structure catalysts were successfully prepared.

Subsequently, X-ray spectroscopy was used to probe the microstructure and chemical state information of the samples. Firstly, the surface elemental valence and bonding information of the samples were investigated using X-ray photoelectron spectroscopy (XPS). In the C 1*s* high-resolution spectrum, the peaks at 284.8 eV, 285.6 eV, and 288.9 eV can be attributed to C=C bonding, C=N/C-N bonding, and C-O bonding, respectively (**Fig. S27**)[18, 43]. For the N 1*s* high-resolution spectra, the peaks at about 398.4 eV, 399.1 eV, 400.5 eV, 401.4 eV and 403.7 eV can be attributed to pyridine-N, metal-N, pyrrole-N, graphite-N and oxidative-N species, respectively (**Fig. S28**)[9, 17, 41]. It can be found that the percentage of metal-N in the series of samples containing *p*-block metals is slightly enhanced relative to that of Mn-NC (**Fig. S29**), which, combined with the AC-HAADF-STEM results and the ICP-OES results, can be deduced to be the contribution from the increase of the metal single-atom sites. The pyridine-N is also thought to contribute to the ORR activity [46]. It can be found all the MnM-NC catalysts have similar composition of N and C, indicating that the N-doped carbon matrix across different catalysts have similar structure. For the XPS spectra of Mn 2p, the 2p3/2 peaks of the samples doped with *p*-block metals show a slight

negative shift compared with Mn-NC, indicating the Mn in MnM-NC gains more electrons from coordinated N (**Fig. S30**).

To further reveal the atomic coordination structure of the catalysts, X-ray absorption energy near edge structure (XANES) spectroscopy and extended X-ray absorption fine structure (EXAFS) spectroscopy were applied. In the Mn *K*-edge XANES spectra (**Fig. 3a**), the absorption edges of the Mn-NC and MnGa-NC samples are located between the MnO(II) and Mn_2O_3(III), and are closer to MnO, suggesting that the Mn in the catalysts has a mixed valence state that is closer to Mn(II). The average valency of Mn in Mn-NC is estimated to be +2.45, and decreased to +2.38 for MnGa-NC (**Fig. S31**), which aligns with the XPS results. In the Fourier transformed (FT)-EXAFS spectra of Mn *K*-edge in *R*-space (**Fig. 3b**), for the sample Mn-NC, a strong peak at about 1.3 Å is attributed to the coordination scattering of Mn-N as well as Mn-C. For MnGa-NC, in addition to the major Mn-N peak at 1.3 Å, there is a small peak at 2.4 Å, which can be assigned to dual-single-atom sites, such as Mn-Ga. For both samples, no Mn-O peak is detected at 1.5 Å, and no significant Mn-Mn scattering path is detected at 2.3 Å. This suggests the atomic dispersion of Mn in the samples without the formation of oxide particles or metal clusters, which is further confirmed by the wavelet transforms of FT k^3-weighted EXAFS spectra at Mn K-edge (**Fig. S32**). The *R*-space of the Mn *K*-edge was further fitted for Mn-NC and MnGa-NC. For Mn-NC (**Fig. S33-34**), the dominant scattering path is Mn-N, and the model (inset in **Fig. S33**) matches the fitting well; while for MnGa-NC (**Fig. 3c, S35**), the overall N coordination number is still about 4 but the coordinated N is a little different due to the asymmetric structure. It is worth noting that the Mn-Ga scattering paths make huge contributions to a good fitting (**Table S2**). The XANES spectra of Ga *K*-edge show that the adsorption edges of Ga-NC and MnGa-NC are close to the Ga_2O_3 reference, demonstrating a relatively high valency of Ga, and the absorption edge of MnGa-NC is also negatively shifted compared with Ga-NC (**Fig. 3d**). Referring to the *R*-space spectra of Ga_2O_3 and reported Ga foil[47], in the *R*-space spectrum of the MnGa-NC catalyst, the Ga-Ga peak is absent, whereas the main peak appears at 1.4 Å and an additional small peak at around 2.4 Å can be found, which are speculated to be Ga-N and Ga-Mn scattering, respectively (**Fig. 3e**). Since the main peak Ga-N is very close to Ga-O peak (**Fig. 3e**), wavelet transforms for FT k^3-weighted EXAFS spectra at Ga K-edge were performed to distinguish them (**Fig. 3g-i**), which suggest that the Ga element in MnGa-NC is atomically coordinated with N atoms and no Ga oxides are formed. A fine fitting was also done for MnGa-NC and Ga-NC at Ga *K*-edge (**Fig. 3f, S36-38**), and the peak around 2.4 Å for MnGa-NC is similarly **attributed to the scattering between Mn-Ga (Table S3). From** the EXAFS results of both Mn *K*-edge and Ga *K*-edge, it can be concluded that the Mn-Ga scattering path plays an irreplaceable role in the fitting of MnGa-NC sample, implying that such Mn-Ga dual-single-atom sites exist in the catalyst. In summary, the above analyses demonstrate Mn and Ga are atomically dispersed in MnGa-NC and the dual-single-atom structure of Mn-Ga is reasonably existed in MnGa-NC.

2.2 Electrocatalytic ORR performance

The electrochemical ORR activity of all samples was evaluated in 0.1 M KOH electrolyte using rotating disk electrode (RDE). Linear sweep voltammetry (LSV) curves (**Fig. 4a**) show that the NC catalyst exhibited the worst activity ($E_{1/2}$=0.753 V vs. RHE). In contrast, Mn-NC demonstrated significant

performance enhancement ($E_{1/2}$=0.821 V vs. RHE), indicating the existence of highly active sites such as Mn-N_4 moiety. After introducing *p*- block metal single atoms into Mn-NC, the $E_{1/2}$ was further improved by around 30 mV, rivaling the commercial 20wt% Pt/C ($E_{1/2}$=0.844 V vs. RHE). It is noted that these three kinds of *p*-block meals induce similar activity enhancement. This suggests that synergistic coupling between *p*-block metals and Mn centers facilitates oxygen intermediate adsorption/desorption. Tafel slope analysis (**Fig. 4b**) reveals that Mn-NC already exhibits superior kinetics to 20 wt% Pt/C, with further kinetic enhancement upon *p*-metal incorporation. These catalysts containing *p*-block metals showed higher current densities at 0.8 V(J_k) than Pt/C, indicating accelerated reaction kinetics (**Fig. 4c**). Electrochemical double-layer capacitance (C_{dl}) measurements (**Fig. 4d, S39**) revealed that introducing *p*-block metals can improve the electrocatalytic active surface area, and the specific activities were also improved (**Fig. S40**), which imply that the incorporation of *p*-block metals can expose more active sites as well as increase the intrinsic activity. Rotating ring disk electrode (RRDE) measurements (**Fig. 4e, S41**) showed that the Ga-optimized catalysts can maintain electron transfer number (n) ≈3.95 and HO_2^- yield <5% across wide potentials, indicating dual-single-atom configurations favor $4e^-$ pathways. LSV curves at different rotational speeds (625-2025 rpm) were also tested and the number of transferred electrons was calculated based on the K-L equation (**Fig. S42-46**), the results of which were in general agreement with the RRDE tests.

The stability of the catalyst was tested accordingly. MnGa-NC exhibited exceptional stability with about 90% current retention after 40,000 s chronoamperometry test at 0.75 V vs. RHE (**Fig. 4f**), outperforming commercial 20wt% Pt/C (87% retention). MnIn-NC and MnSn-NC also exhibited >90% current retention, outperforming Mn-NC and NC (**Fig. S47**). Moreover, accelerated cyclic voltammetry tests show that Mn-NC (**Fig. S48**) and MnM-NC (**Fig. 4g-i**) catalysts demonstrate superior stability to the commercial 20wt% Pt/C even under high loading amount (**Fig. S49-50**). Methanol resistance test shows that (**Fig. S51**), which is important for direct methanol fuel cells, *p*-block metal doped catalysts exhibited good resistance to methanol compared with Mn-NC, while the oxygen reduction efficiency of commercial Pt/C significantly decreased in the presence of methanol.

2.3 Theoretical calculations

To gain a deeper theoretical understanding of the origins of the oxygen reduction activity of *p*-block metal-doped Mn-N-C catalysts, density function theory (DFT) simulations were performed by modeling Mn-N_4, Ga-N_4 and the coupling-generated MnGa-N_6 on the graphene network structure (**Fig. S52-59**). We use Ga as a representative *p*-block metal for preliminary theoretical analysis. Initially, both the association mechanism (**Fig. 5a, S60**) and the dissociative mechanism of the ORR process are considered (**Fig. S61**), but it was found the former is more likely to occur. Therefore, the following discussions are based on the association mechanism. The adsorption energies of each intermediate for the three structural models are calculated by setting the potential at U=1.23 V (**Fig. 5b**). For Ga-N_4, its extremely high *OH adsorption strength hinders the H_2O generation in the last step, which in turn hinders the regeneration of active sites, resulting in low ORR performance. For the Mn-N_4 structure, similarly, the protonation desorption process of *OH needs to overcome the maximum energy barrier and thus is the rate

determining step (RDS) of the overall reaction. Comparing to Mn-N_4, the introduction of Ga, i.e., the MnGa-N_6 model, facilitates both the transition from *O to *OH as well as *OH to H_2O, and more importantly, weakens the *OH adsorption strength, thus facilitating the overall reaction process.

Subsequently, to reveal the specific origin of activity in the gallium-containing samples, we calculated the projected density of the *p*-orbitals of Ga and the *d*-orbitals of Mn. It is found that the *d*-*p* orbital hybridization originates from the partial overlap of energies between their *d*-*p* orbitals (**Fig. 5c, Fig. S62**). Comparison of the *d*-band center of metal Mn in Mn-N_4 and modified MnGa-N_6 reveals that the *d*-band center is downshifted from the original -2.156 eV to -2.238 eV after introducing Ga (**Fig. 5d, S63**). According to the *d*-band center theory[48], the downshift of the *d*-band center can alleviate the over-adsorption of oxygen species and facilitate the overall reaction process. Although In and Sn differ from Ga in their electronic structures, they also exhibit strong *p*-*d* orbital hybridization with Mn (**Fig. S64–65**). Further theoretical calculations indicate that all three *p*-block metal-doped catalysts have a reduced RDS (*OH → H_2O) energy barrier under *p*-*d* hybridization (**Fig. S66**). The charge density difference map can visually reveal the high-density electron enrichment on the Mn sites, which is favorable to the adsorption and activation of O_2. Through the quantitative calculation of Bader charge, Mn and Ga in MnGa-N_6 get more electrons compared to the Mn in Mn-N_4 and Ga in Ga-N_4, respectively, which is consistent with the XAS and XPS results. The Mn and Ga atoms in MnGa-N_6 gain additional 0.021 and 0.013 electrons, respectively, which are thought to come from the co-transfer of the surrounding nitrogen (**Fig. 5e-f, Table S4**). In summary, the introduction of *p*-block metals can adjust the *d*-band center of Mn center and optimize the adsorption of oxygen species.

4. Conclusions

In summary, we have synthesized a series of Mn single-atom electrocatalysts for ORR, which are characterized by the dual-single-atom structure composed of Mn sites and *p*-block metals (Ga, In, and Sn). Experimental characterizations and theoretical modeling demonstrate the coupling between the *d* orbital of Mn and the *p* orbital of *p*-block metals. After introducing *p*-block metals, the ORR activity was improved and comparable with commercial Pt/C. DFT calculations show that the introduction of *p*-block metals can adjust the *d*-band center of Mn single-atom site, modulate the adsorption and desorption strengths of oxygen species, and lower the RDS energy barriers, thereby improving ORR kinetics. All the MnM-NC catalysts exhibited good catalytic stability that is superior to commercial Pt/C. We expect that this work will inspire more innovative works on *p*-block metals in the field of ORR.

Author contributions

Yujie Cui and Yihong Liu contributed equally to this work. Yujie Cui did most of the experiments, analyse the data and wrote the original draft; Yihong Liu conducted DFT calculations; Jiayi Li, Haibin Ma, Tingting Pan, Hainan Wei, Xinyue Shi, Xiaoyan Zhou, Ping Zhang, Weixing Niu, Shengnan Sun, Menghao Yang provided guidance on the DFT calculations, Wei-Hsiang Huang provided resources for X-ray absorption investigation and supervised on the data analysis. Jiwei Ma provided guidance on the methodology and supervision. Funding

acquisition. Hongfei Cheng conceived the idea and supervised on the whole project. All authors contributed to the writing review & editing.

Conflicts of interest

The authors agree that there is no interest conflicts need to be declare.

Data availability

The data supporting this article have been included as part of the Supplementary Information.

Acknowledgements

This work was funded by the National Natural Science Foundation of China (22405191), Natural Science Foundation of Shanghai Municipality (24ZR1468100) and the Fundamental Research Funds for the Central Universities to H.C.. We thank National Synchrotron Radiation Research center (beamline TLS 17C and TPS 44A) for the allocation of synchrotron beam time under Proposal No. 2024-2-027-1.

References

1. L. Chen, X. Xu, W. Yang and J. Jia, *Chinese Chemical Letters*, 2020, **31**, 626–634.
2. K. Jiao, J. Xuan, Q. Du, Z. Bao, B. Xie, B. Wang, Y. Zhao, L. Fan, H. Wang, Z. Hou, S. Huo, N. P. Brandon, Y. Yin and M. D. Guiver, *Nature*, 2021, **595**, 361–369.
3. *Journal of Electrochemistry*, 2024, **30**, 2024121.
4. T. H. Dolla, S. P. Mbokazi, T. Matthews, R. Mohamed, L. L. Sikeyi, U. M. Tukur, J. Wang, P. F. Msomi, W. K. Maboya, P. R. Makgwane, N. Palaniyandy and M. K. Mathe, *Energy Storage Materials*, 2025, **79**, 104357.
5. L. Gong, J. Zhu, F. Xia, Y. Zhang, W. Shi, L. Chen, J. Yu, J. Wu and S. Mu, *ACS Catalysis*, 2023, **13**, 4012–4020.
6. M. Liu, Z. Zhao, X. Duan and Y. Huang, *Advanced Materials*, 2018, **31**, 1802234.
7. C. Zhang, Q. Zhang, Y. Hu, H. Hu, J. Yang, C. Yang, Y. Zhu, Z. Tu and D. Wang, *Chinese Chemical Letters*, 2024, **36**, 110429.
8. W. Song, C. Xiao, J. Ding, Z. Huang, X. Yang, T. Zhang, D. Mitlin and W. Hu, *Advanced Materials*, 2023, **36**, 2301477.
9. T. Shen, X. Huang, S. Xi, W. Li, S. Sun and Y. Hou, *Journal of Energy Chemistry*, 2022, **68**, 184–194.
10. H. Niu, L. Huang, Y. Qin, R. Qi, B. Mei, D. Wu, F.-M. Li, B. You, Q. Li, Y. Yao, Z. Wang, T. Yao, S. Ding, W. Guo, Y. Chen, Y. Su, F. Song and B. Y. Xia, *Journal of the American Chemical Society*, 2024, **146**, 22650–22660.
11. S. Liu, T. Zeng, Z. He, M. Zuo, S. Chen, Y. Liu, Z. Fan, H. He, Q. Kong, Z. Zhou and L. Han, *Chemical Engineering Journal*, 2024, **499**, 156051.
12. L. Yao, W. Yang, H. Liu, J. Jia, G. Wu, D. Liu, T. Liu, T. Tan and C. Wang, *Dalton Transactions*, 2017, **46**, 15512–15519.
13. C. Shi, S. Ullah, K. Li, W. Wang, R. Zhang, L. Pan, X. Zhang and J.-J. Zou, *Chinese Journal of Catalysis*, 2020, **41**, 1818–1825.

14. X. Zhong, M. h. Oubla, X. Wang, Y. Huang, H. Zeng, S. Wang, K. Liu, J. Zhou, L. He, H. Zhong, N. Alonso-Vante, C.-W. Wang, W.-B. Wu, H.-J. Lin, C.-T. Chen, Z. Hu, Y. Huang and J. Ma, *Nature Communications*, 2021, **12**, 3136.

15. X. Zhong, L. Sui, M. Yang, T. Koketsu, M. Klingenhof, S. Selve, K. G. Reeves, C. Ge, L. Zhuang, W. H. Kan, M. Avdeev, M. Shu, N. Alonso-Vante, J.-M. Chen, S.-C. Haw, C.-W. Pao, Y.-C. Chang, Y. Huang, Z. Hu, P. Strasser and J. Ma, *Nature Catalysis*, 2024, **7**, 546–559.

16. K. Liu, Z. Qiao, S. Hwang, Z. Liu, H. Zhang, D. Su, H. Xu, G. Wu and G. Wang, *Applied Catalysis B: Environment and Energy*, 2018, **243**, 195–203.

17. M. Tong, F. Sun, G. Xing, C. Tian, L. Wang and H. Fu, *Angewandte Chemie International Edition*, 2023, **62**, 202314933.

18. J. Li, M. Chen, D. A. Cullen, S. Hwang, M. Wang, B. Li, K. Liu, S. Karakalos, M. Lucero, H. Zhang, C. Lei, H. Xu, G. E. Sterbinsky, Z. Feng, D. Su, K. L. More, G. Wang, Z. Wang and G. Wu, *Nature Catalysis*, 2018, **1**, 935–945.

19. H.-J. Zhang, B. Chen, C. Cai, T. Yuan, L. Sun and Y. Xue, *Energy & Fuels*, 2021, **35**, 16822–16828.

20. X. Zhang, F. Yang, S. Sun, K. Wei, H. Liu, G. Li, Y. Sun, X. Li, J. Qian, S. Du, M. Li, Y. Lu, C. Xia, S. Che and Y. Li, *Journal of Colloid and Interface Science*, 2023, **657**, 240–249.

21. L. Guo, S. Hwang, B. Li, F. Yang, M. Wang, M. Chen, X. Yang, S. G. Karakalos, D. A. Cullen, Z. Feng, G. Wang, G. Wu and H. Xu, *ACS Nano*, 2021, **15**, 6886–6899.

22. Y. Li, H.-R. Wu, Y. Yu, M.-Y. Chen, K.-M. Zhao, W.-D. Li, S.-Y. Rong, D.-P. Xue, J.-N. Zhang and B.-A. Lu, *Small*, 2025, **21**, 2411678.

23. J. Huo, X. Cao, Y. Tian, L. Li, J. Qu, Y. Xie, X. Nie, Y. Zhao, J. Zhang and H. Liu, *Nanoscale*, 2023, **15**, 5448–5457.

24. X. Lin, D. Liu, L. Shi, F. Liu, F. Ye, R. Cheng and L. Dai, *Small*, 2024, 2407146.

25. Y. Yang, K. Mao, S. Gao, H. Huang, G. Xia, Z. Lin, P. Jiang, C. Wang, H. Wang and Q. Chen, *Advanced Materials*, 2018, **30**, 1801732.

26. J. Bai, Y. Fu, P. Zhou, P. Xu, L. Wang, J. Zhang, X. Jiang, Q. Zhou and Y. Deng, *ACS Applied Materials & Interfaces*, 2022, **14**, 29986–29992.

27. H. Cai, G. Zhang, X. Zhang, B. Chen, Z. Lu, H. Xu, R. Gao and C. Shi, *Small*, 2022, **18**, 2200911.

28. C. Hu, G. Xing, W. Han, Y. Hao, C. Zhang, Y. Zhang, C. H. Kuo, H. Y. Chen, F. Hu, L. Li and S. Peng, *Advanced Materials*, 2024, **36**, 2405763.

29. L. Ran, Y. Xu, X. Zhu, S. Chen and X. Qiu, *ACS Nano*, 2023, **18**, 750–760.

30. Y. Zhao, Z. Gao, S. Zhang, X. Guan, W. Xu, Y. Liang, H. Jiang, Z. Li, S. Wu, Z. Cui and S. Zhu, *Advanced Functional Materials*, 2025, 2504260

31. H. Hu, P. Zhang, B.-B. Xiao and J.-L. Mi, *Catalysis Science & Technology*, 2022, **12**, 6751–6760.

32. S. H. Mohd Chachuli, S. N. Timmiati, K. S. Loh, W. Y. Wong, K. L. Lim and R. M. Yunus, *Journal of Industrial and Engineering Chemistry*, 2025, **149**, 176–208.

33. H. Wang, X. Niu, W. Liu, R. Yin, J. Dai, W. Guo, C. Kong, L. Ma, X. Ding, F. Wu, W. Shi, T. Deng and X. Cao, *Advanced Science*, 2024, **11**, 2403865.

34. L. Zhao, Y. Dai, Y. Zhang, B. Liu, P. Guo, Z. Zhang, L. Shen, N. Zhang, Y. Zheng, Z. Zhang, Z. Wang and Z. Chen, *Angewandte Chemie International Edition*, 2024, **63**, 202402657.

35. Y. Xu, S. Chen, L. Chen, X. Zhu, X. Qiu and M. Liu, *The Journal of Physical Chemistry Letters*, 2023, **14**, 5850–5859.

36. D. Deng, S. Wu, H. Li, H. Li and L. Xu, *Small*, 2022, **19**, 2205469.

37. F. Luo, A. Roy, L. Silvioli, D. A. Cullen, A. Zitolo, M. T. Sougrati, I. C. Oguz, T. Mineva, D. Teschner, S. Wagner, J. Wen, F. Dionigi, U. I. Kramm, J. Rossmeisl, F. Jaouen and P. Strasser, *Nature Materials*, 2020, **19**, 1215–1223.

38. J. Yu, X. Yong and S. Lu, *Energy & Environmental Materials*, 2023, **7**, 12587.

39. P. Li, J. Bi, J. Liu, Y. Wang, X. Kang, X. Sun, J. Zhang, Z. Liu, Q. Zhu and B. Han, *Journal of the American Chemical Society*, 2023, **145**, 4675–4682.

40. V. Krishnamoorthy, P. Sabhapathy, P. Raghunath, C. Y. Huang, A. Sabbah, M. K. Hussien, Z. Syum, S. Muthusamy, M. C. Lin, H. L. Wu, R. S. Chen, K. H. Chen and L. C. Chen, *Small Methods*, 2024, **8**, 2301674.

41. X. Wang, N. Zhang, S. Guo, H. Shang, X. Luo, Z. Sun, Z. Wei, Y. Lei, L. Zhang, D. Wang, Y. Zhao, F. Zhang, L. Zhang, X. Xiang, W. Chen and B. Zhang, *Journal of the American Chemical Society*, 2024, **146**, 21357–21366.

42. J. Chen, T. Zhou, C. He, Z. Luo, C. Shi, L. Zhang, Q. Zhang, C. He and X. Ren, *Nanoscale*, 2024, **16**, 21515–21522.

43. Y. Liu, J. Li, Z. Lv, H. Fan, F. Dong, C. Wang, X. Chen, R. Liu, C. Tian, X. Feng, W. Yang and B. Wang, *Journal of the American Chemical Society*, 2024, **146**, 12636–12644.

44. S. An, L. Wang and Q. Jin, *Journal of Water Process Engineering*, 2024, **58**, 104907.

45. C. Zhu, Q. Shi, B. Z. Xu, S. Fu, G. Wan, C. Yang, S. Yao, J. Song, H. Zhou, D. Du, S. P. Beckman, D. Su and Y. Lin, *Advanced Energy Materials*, 2018, **8**, 1801956.

46. N. Xue, J. Yin, X. Xue, H. Zhu and J. Yin, *Journal of Materials Chemistry A*, 2024, **12**, 31630–31637.

47. C. Zhou, J. Shi, Z. Dong, L. Zeng, Y. Chen, Y. Han, L. Li, W. Zhang, Q. Zhang, L. Gu, F. Lv, M. Luo and S. Guo, *Nature Communications*, 2024, **15**, 6741.

48. A. Kulkarni, S. Siahrostami, A. Patel and J. K. Nørskov, *Chemical Reviews*, 2018, **118**, 2302–2312.

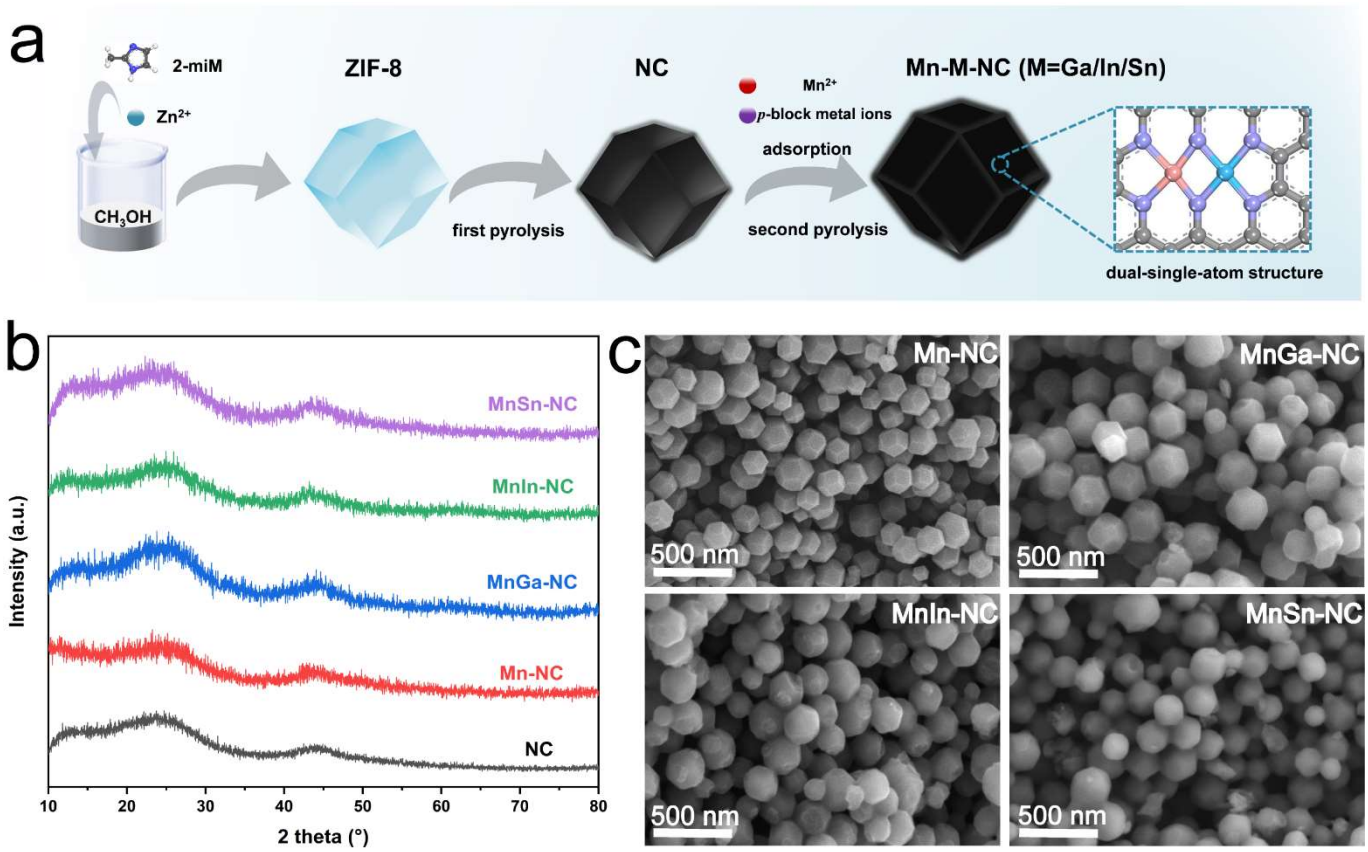

Fig. 1 (a) Schematic diagram of the preparation process of catalysts with dual-single-atom structure. **(b)** XRD patterns of NC, Mn-NC, MnGa-NC, MnIn-NC and MnSn-NC catalysts. **(c)** SEM images of Mn-NC, MnGa-NC, MnIn-NC and MnSn-NC.

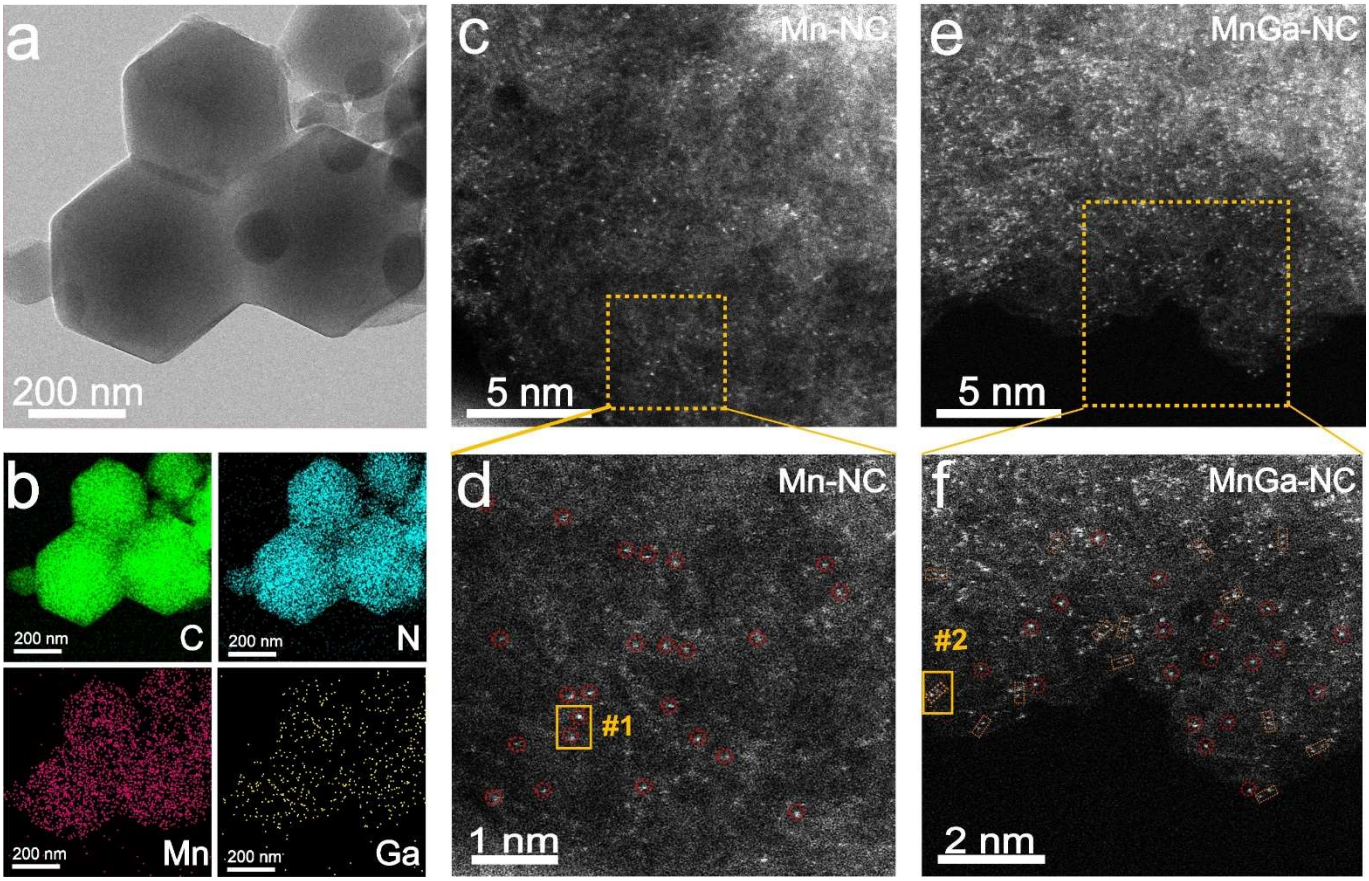

Fig. 2 (a) TEM image of MnGa-NC. **(b)** EDS elemental mapping of MnGa-NC catalyst. **(c)** HAADF-STEM image of Mn-NC. **(d)** The enlarged region in **c**, with single-atomic sites at the red dashed circle. **(e)** HAADF-STEM image of MnGa-NC. **(f)** The enlarged region in **e**, with single-atomic sites at the red dashed circle and potential dual-single-atom sites at the orange dashed rectangle.

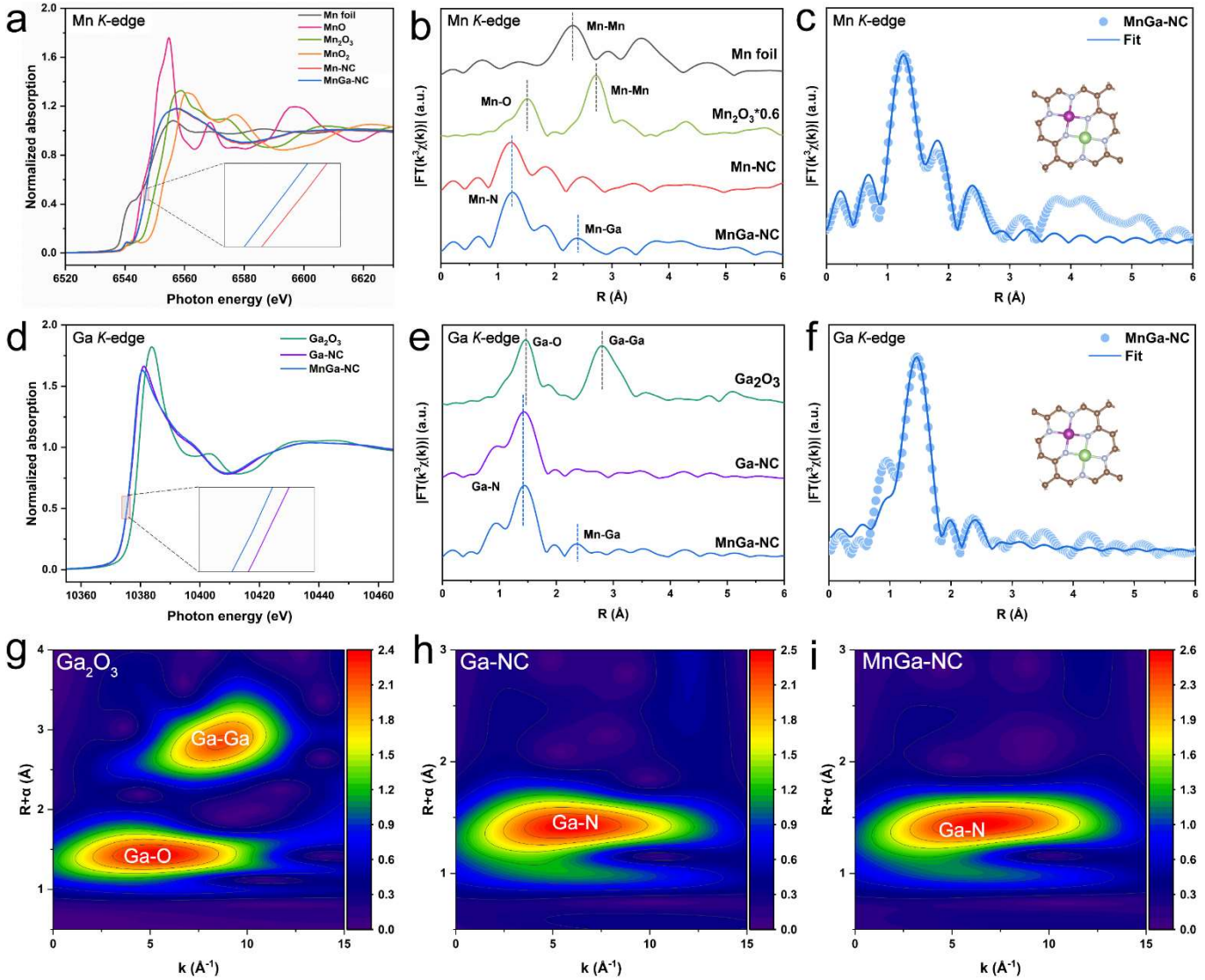

Fig. 3 (a) The normalized Mn *K*-edge XANES spectra. **(b)**The Fourier transform of k^3-weighted EXAFS spectra of Mn-NC, MnGa-NC and related references at Mn *K*-edge. **(c)** EXAFS fitting curve in *R*-space of MnGa-NC at Mn *K*-edge (inset is the fitted model, with purple atoms for Mn, proto-green atoms for Ga, silver-grey atoms for N, and brown atoms for C). **(d)** The normalized Ga *K*-edge XANES spectra. **(e)** The Fourier transform of k^3-weighted EXAFS spectra of Ga-NC, MnGa-NC and related references at Ga *K*-edge. **(f)** EXAFS fitting curve in *R*-space of MnGa-NC at Ga *K*-edge. WT for FT k^3-weighted EXAFS spectra of **(g)** Ga_2O_3, **(h)** Ga-NC, and **(i)** MnGa-NC at the Ga *K*-edge.

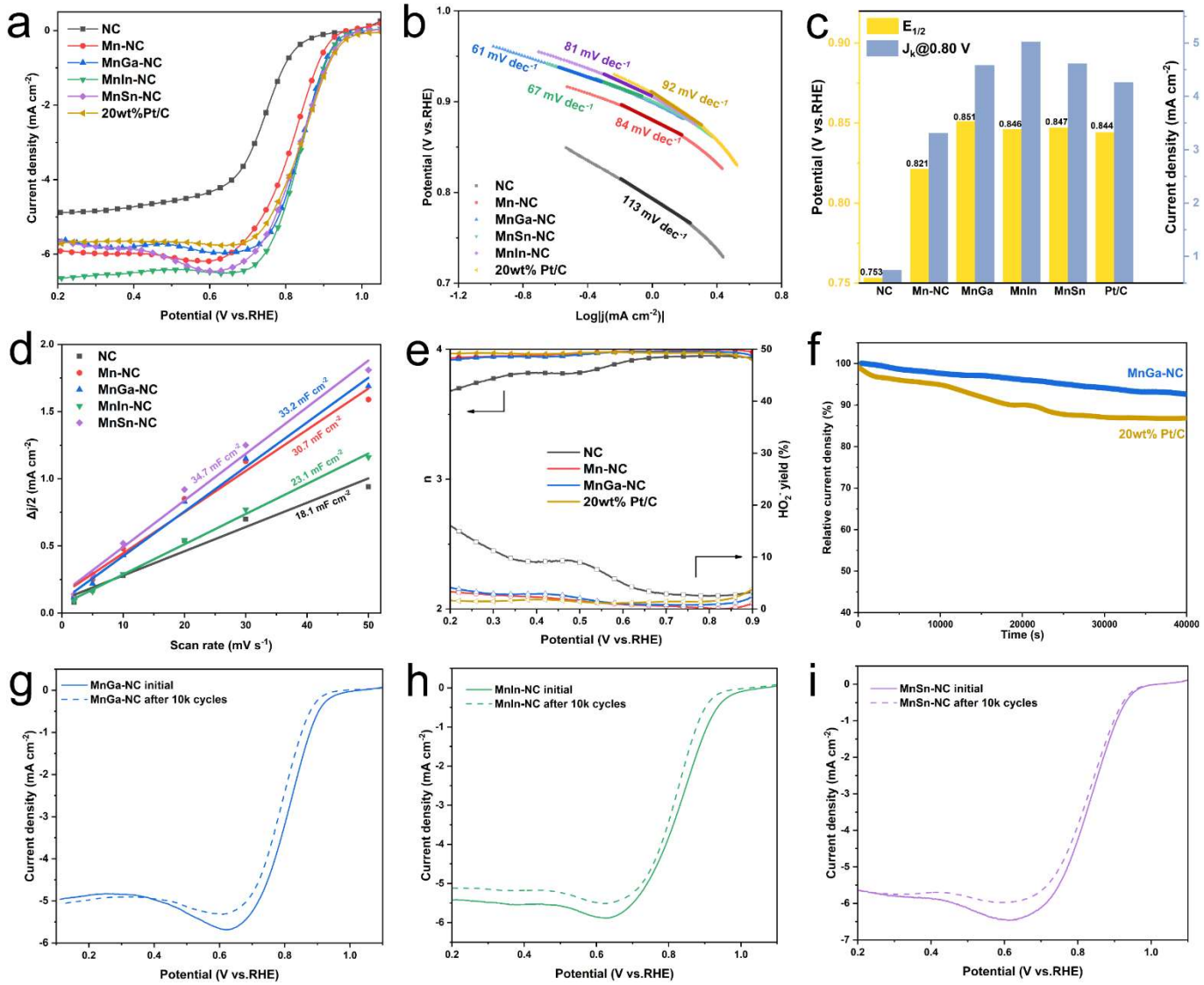

Fig. 4 (a) Comparison of LSV polarization curves for various catalysts in 0.1 M KOH. **(b)** Tafel plots for various catalysts. **(c)** The kinetic current densities at 0.80 V vs. RHE and $E_{1/2}$ (half-wave potential) for various catalysts. **(d)** Electrochemical double-layer capacitance measurements of various catalysts. **(e)** Electron transfer number and HO_2^- yield in ORR process of various catalysts. **(f)** The i-t test of MnGa-NC and 20wt% Pt/C. **(g-i)** ADT (accelerated durability test) for MnGa-NC, MnIn-NC and MnSn-NC.

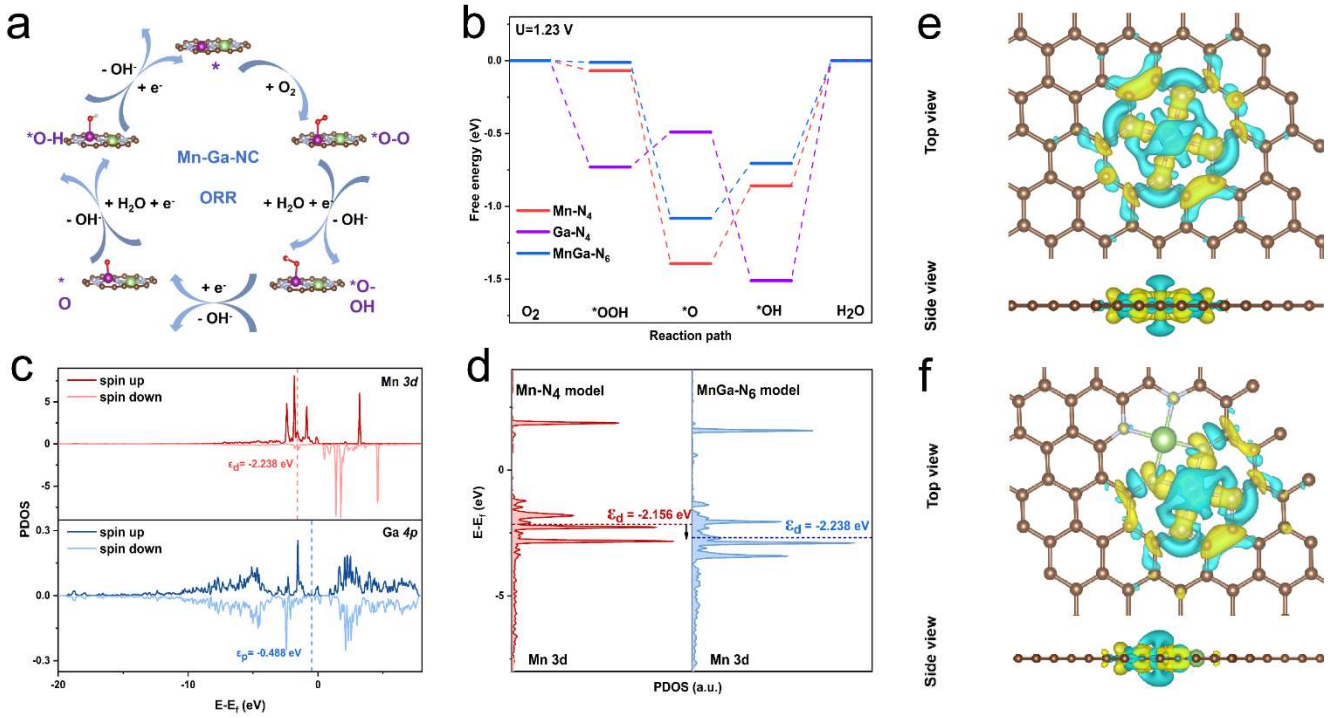

Fig. 5 (a) The diagram of ORR mechanism on the MnGa-NC active site in the alkaline environment, in which brown atoms represent carbon atoms, silver-grey atoms represent nitrogen atoms, purple atoms represent manganese atoms and green represents gallium atoms. **(b)** Comparison of the step diagrams of the oxygen reduction process on the Mn-N_4, Ga-N_4, MnGa-N_6 site. **(c)** Calculation of the PDOS of the 3*d* orbitals of Mn and the 4*p* orbitals of Ga in the MnGa-N_6 model. **(d)** Comparison of the calculation of the *d*-band center of Mn in Mn-N_4 and MnGa-N_6. **(e-f)** Schematic diagrams of differential charge densities on the sites of Mn-N_4 and MnGa-N_6, with the yellow area representing the accumulation of electrons and the blue area representing the loss of electrons.